🔓Open Access

Integrated Photonic Platform for Robust Differential Refractive Index Sensor

André L. Moras
Valnir Silva
Mario C. M. M. Souza
Giuseppe A. Cirino
Antônio A. G. Von Zuben
Luis A. M. Barea
Newton C. Frateschi
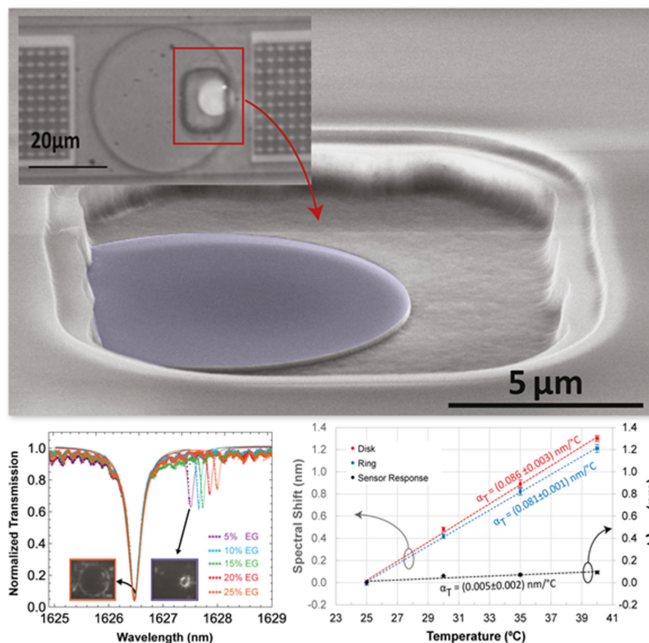
![IEEE photonics SOCIETY logo] ![IEEE logo]

Integrated Photonic Platform for Robust Differential Refractive Index Sensor

André L. Moras [ORCID],[1] **Valnir Silva,**[2] **Mario C. M. M. Souza,**[1]
Giuseppe A. Cirino,[2] **Antônio A. G. Von Zuben,**[1] **Luis A. M. Barea,**[2]
and Newton C. Frateschi [ORCID][1]

[1]Gleb Wathagin Physics Institute, University of Campinas, 13083-859 Campinas, SP, Brazil
[2]Department of Electrical Engineering, Federal University of São Carlos, 13565-905 São Carlos, SP, Brazil

Abstract: We demonstrate an integrated photonic platform comprising a refractive index (RI) sensor based on Photonic Molecule (PM) that effectively mitigates the influence of environmental perturbations using a differential measurement scheme while providing high quality-factor (Q) resonances. The RI sensor consists of a partially unclad microdisk resonator coupled to an external clad microring resonator fabricated on silicon-on-insulator (SOI) platform. We report a RI sensitivity of 24 nm/RIU, achieving a limit of detection (LOD) of 1.7×10^{-3} refractive index units (RIU) with improved stability for an operation range of 0.15 RIU in a compact footprint of $40 \times 40 \ \mu m^2$, representing an important solution for real-life applications in which measurement conditions are not easily controllable.

Index Terms: Optical sensing and sensors, Sensor, Integrated optics devices.

1. Introduction

In the past decades, there have been enormous advances in the research of silicon-on-insulator (SOI)-based integrated optical microcavities fueled by the high scientific interest and technological demands in several areas including optical communications and optical sensing [1]–[4]. These optical microcavities, such as rings or disks, permit strong light confinement and their dimensions can be adjusted for a given desired spectrum and application [2], [5]. When these microcavities are fabricated on SOI platform, the tight light confinement within the microcavities allows them to be ultra-compact and easy to integrate with other devices [2], [4]. Harnessing these advantages, the cavities can compose very large scale integrated optoelectronic circuits, fabricated by mature microfabrication technology based on complementary metal-oxide-semiconductor (CMOS) [6]. In particular, these cavities also ensure high sensitivity to refractive index (RI) changes and potential integration with microfluidic applications [3], [7]–[10], allowing the implementation of gas, temperature and biological material sensing functionalities on a single chip, the so-called lab-on-a-chip (LOC) [8], [11], [22], which promotes significant advances in fundamental areas such as environmental monitoring and biomedicine [23]–[27].

Several studies in the literature show the efficiency of SOI microcavities coupled to waveguides to monitor dynamic molecular reactions, quantitative concentrations of solutions and to determine chemical affinities for medical studies and clinical diagnosis [4], [8], [28]. These studies usually show that a microcavity can be used as an optical sensor in homogeneous sensing approach when the analytes, suspended in a fluid medium, are covering the microcavity top. In this situation, the effective refractive index (n_{ef}) of the cavity mode will change, resulting in a corresponding deviation of the resonant wavelength, guaranteeing the sensing capacity [2], [7], [11]. However, most optical devices exhibit some vulnerability to temperature variations and it is no different with microcavities-based sensors. Environmental disturbances, especially temperature variations, induce spurious changes in resonant wavelength and should be controlled or avoided to improve the detection limit of these sensors. Several solutions to overcome temperature sensitivity have been proposed using materials with negative thermo-optic coefficients as cavity claddings, external temperature compensating devices, active control of device temperature and differential measurements employing various cavities and microfluidic channels [12]-[21]. All of these solutions suffer to satisfy the CMOS fabrication process rules as well as increase power consumption and require a larger chip area. To overcome these limitations, we present in this work a CMOS-integrated photonic platform comprising a compact RI sensor based on a Photonic Molecule (PM), capable of decreasing the temperature-dependence of the sensor to 0.005 nm/°C by employing differential measurement between the resonances of the PM's cavities, without requiring greater fabrication complexity and increasing the footprint area. This result corresponds to a temperature-induced resonant wavelength shift of only 0.5 nm over an operating temperature range of 100°C, which is approximately 16 times smaller than the resonant shift experienced by a single Si microring resonator subjected to the same temperature shift.

2. Theory and Modeling

In general, when a single ring or disk resonator is used as a RI sensor, the limit of detection (LOD) [7], which indicates the minimum detectable concentration changes in the sensor, is measured in RIU and can be defined as:

$$LOD = \frac{\lambda_{res}}{Q\, S_{RI}} \tag{1}$$

where λ_{res} is the resonant wavelength responsible for detection, Q is the quality factor and S_{RI} is the RI sensitivity, defined as [7], [29], [30]:

$$S_{RI} = \frac{\Delta\lambda_{res}}{\Delta n_c} \tag{2}$$

where $\Delta\lambda_{res}$ is the change in the resonant wavelength due to the change in the cladding RI over the cavity (Δn_c). In this class of sensors, a small LOD is desired so that small variations in n_c can be detected by a deviation in $\Delta\lambda_{res}$. In fact, when the cladding RI (n_c) is changed, the n_{ef} of the resonator also undergoes a change, so that for a small wavelength range, the change in n_{ef} (Δn_{ef}) is practically proportional to Δn_c:

$$\Delta n_{ef} = K.\Delta n_c \tag{3}$$

The parameter K is a constant and it depends on the material and waveguide cross-section [2], [7]. In addition, in this type of sensors, the resonance condition of the microcavity imposes that $m\,\lambda_{res} = n_{ef}\,L$, where $L = 2\pi R$ is the perimeter of the resonator, R is the resonator radius and m (positive integer) is the azimuthal resonant order. Thus, any variation in Δn_{ef} can be related to a deviation in $\Delta\lambda_{res}$, giving by:

$$\frac{\Delta n_{ef}}{n_{ef}} = \frac{\Delta\lambda_{res}}{\lambda_{res}} \tag{4}$$
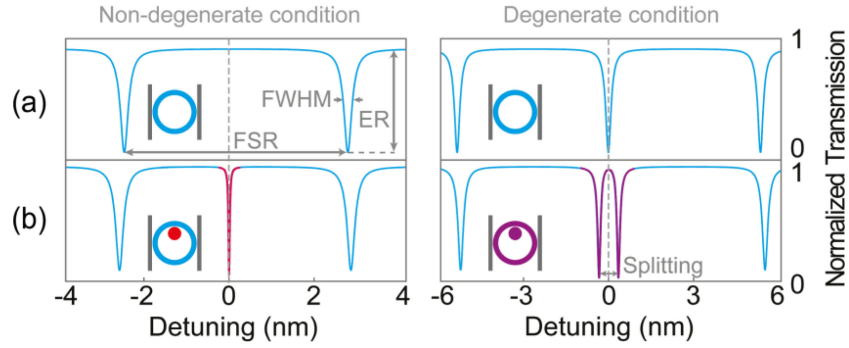
Fig. 1. Comparison between the transmission spectrum of (a) a single microring resonator and (b) a PM based on two coupled resonators, an external ring and an inner disk, for both non-degenerate (left side) and degenerate (right side) conditions. The transmission spectra are shown as a function of the detuning with respect to the embedded disk resonances [33], [34]. The colored resonances are associated with each one of the cavities in the inserted schemes.

and any variation in Δn_c can also be detected by a variation in $\Delta\lambda_{res}$, as suggested by:

$$\Delta n_c = \frac{n_{ef}}{K}\, \frac{\Delta\lambda_{res}}{\lambda_{res}} \tag{5}$$

However, the measurement range of these sensors is dependent of the wavelength shift $\Delta\lambda_{res}$, which is limited by the free spectral range (FSR) of the resonator:

$$\Delta\lambda_{res} < FSR \; = \; \left(\frac{\lambda_{res}^2}{n_g\, L}\right) \tag{6}$$

where n_g is the group index ($n_g = n_{ef} - \lambda\frac{\partial n_{ef}}{\partial \lambda}$). Therefore, the measurement range of n_c is then given by [30]:

$$\Delta n_c < \frac{\lambda_{res}}{KL\left(\frac{n_g}{n_{ef}}\right)} \tag{7}$$

Eq. 7 shows that these sensors based on resonators can only maximize Δn_c reducing the resonator length L, which in turns increases its FSR. In contrast, it was shown in Eq. 1 that to minimize the LOD, high-Q and high-S_{RI} should occur. It is well known that high-Q can be achieved in resonators with long L, since they have low bend losses, and long FSR can only be achieved with reduced L. Therefore, as high-Q, reduced L and long FSR cannot be obtained simultaneously in the conventional sensors based on a single resonator, one solution is to employ PM to overcome this drawback [31].

In the literature, it has been shown that when multiple resonators are coupled internally to a microring, it is possible to build compact PMs [31]–[34]. The complexity of the PM's transmission spectrum will depend on the number of coupled resonators and how they couple to each other. The well-known transmission spectrum of a single microring resonator in an add-drop filter configuration (Fig. 1(a)) presents resonances separated by the FSR, which is inversely proportional to L, and is characterized by the linewidth (FWHM) and the extinction ratio (ER). When a second distinct resonator, such as a disk, is internally coupled to the microring (Fig. 1(b)), the two resonators may have different resonant wavelengths (non-degenerate condition) or they can be both resonant at the same wavelength (degenerate condition), showing that this particular PM guarantees spectral engineering without increasing the chip area. In the non-degenerate condition, the resonances of the outer microring remain unaffected and a new resonance, associated with the embedded
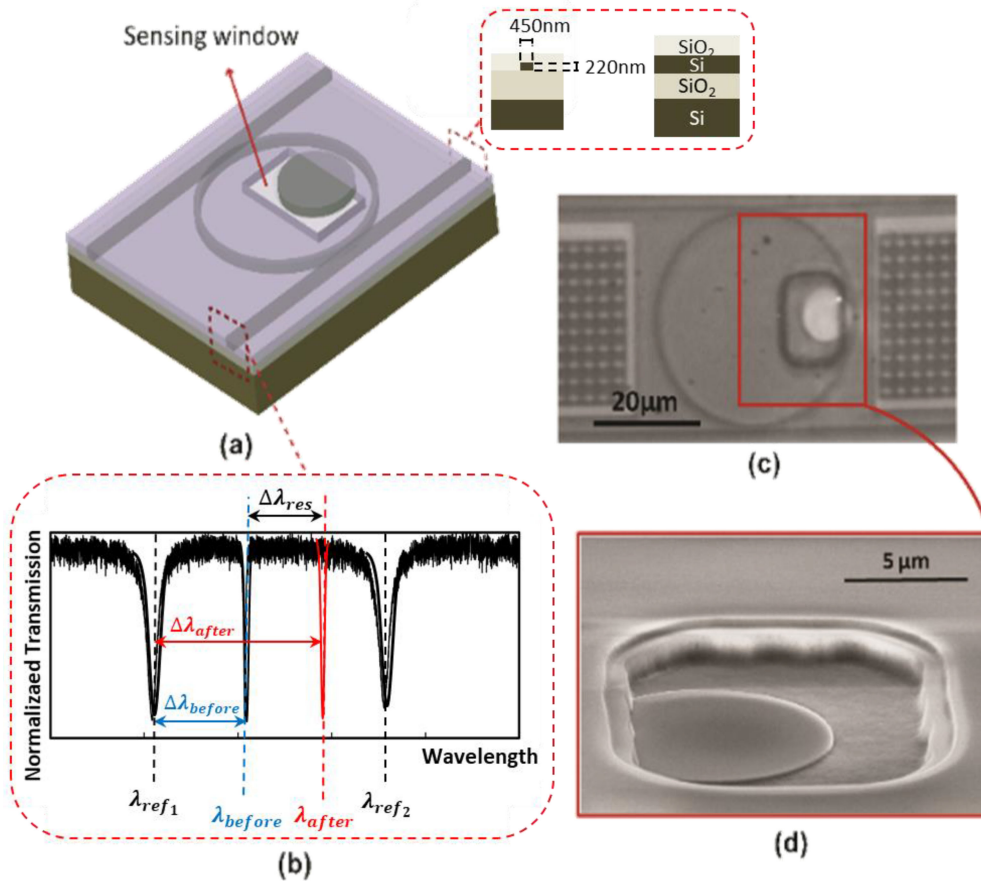
Fig. 2. (a) Schematic view of the sensor based on PM. (b) Desired spectrum for this sensor. The red curve shows a deviation of the disk resonance caused by a change in the cladding refractive index. (c) Optical micrograph of the fabricated sensor and (d) Scanning electron micrograph of the sensing window [33].

disk, appears. However, when the two resonators are degenerated, their mutual coupling induces mode-splitting proportional to the coupling strength between resonators.

Fig. 1(b) shows that in the non-degenerate condition, the notch resonance (red) associated with the embedded disk has a Q higher than the Q associated with the ring resonances. This occurs due to the reduction in the coupling losses between the inner disk and the straight waveguide because the waveguide-disk coupling is always intermediated by the external ring resonances. This way, the non-degenerate approach permits the use of the disk resonance (called detection resonance, $\lambda_{detection}$) for accurate detection, and its wavelength shifts ($\Delta\lambda_{before}$ and $\Delta\lambda_{after}$) may be measured in relation to the ring resonances (called reference resonances, λ_{Ref1} and λ_{Ref2}). These reference resonances should always be present and they need to be fixed and free of deviations caused by the n_c changes, allowing a differential measurement between the detection and reference resonances:

$$\Delta\lambda_{res} = \Delta\lambda_{after} - \Delta\lambda_{before} = \left(\lambda_{detection}^{after} - \lambda_{Ref}^{after}\right) - \left(\lambda_{detection}^{before} - \lambda_{Ref}^{before}\right) \qquad (8)$$

To satisfy this condition, a sensing window must be opened only on the top of the disk (Fig. 2(a)), ensuring that only $\lambda_{detection}$ suffers from the n_c variation. The advantage of computing $\Delta\lambda_{res}$ in this differential method is that it will always be present in the spectra (Fig. 2(b)), even under conditions where there are temperature fluctuations. In fact, high-Q RI sensors are highly sensitive

to fluctuations induced by the environment, such as temperature variations, which compromise their reliability and stability in real-life applications. One solution to overcome this limitation and improve the sensor sensitivity is employing RI sensors based on PMs combined with differential measurements among $\lambda_{detection}$ and the reference resonances (λ_{Ref1} or λ_{Ref2}).

To proof this idea, we present here the design, fabrication and characterization of this RI sensor. The sensing window is open on the top of the disk, exposing 75% of its upper surface, allowing the disk resonance to undergo deviations (Fig. 2(b)) associated with changes in n_c. These deviations can be caused, for instance, by the fluid (air, gas or liquid) that has been applied on the sensing window and may be measured with respect to the ring resonances (λ_{Ref1} or λ_{Ref2}). As discussed before, this combination between the PM and the differential measurement is responsible to improve the sensor stability and reliability, allowing compact footprint area, high-Q resonances and adequate spectral measurement range.

The proposed RI sensor was fabricated by using a SOI platform at IMEC-EUROPRACTICE. The ring and disk radii are 20 μm and 5 μm, respectively. The gaps between waveguide-ring and ring-disk are 200 nm. The effectively single-mode (TE) waveguides consist of a silicon core with 220 nm x 450 nm cross-section on a 2-μm-thick layer of thermally grown SiO_2, covered with a 1-μm thick-deposited SiO_2 layer. All dimensions used are standard on silicon photonic platforms and they have not been optimized to seek records in sensitivity or LOD. The sensing window was defined by photolithography and etching process (Fig. 2(c) and Fig. 2(d)). The chips containing the sensors were cleaved in areas where there were inverse nanotapers for efficient coupling to optical fibers. The polishing technique with focused ion beam (FIB) milling was employed to obtain high-quality mirrors with excellent coupling condition [35]–[37].

3. Simulations

The spectral features of the sensor were carried out using 2-dimensional finite-difference time-domain (2D-FDTD) algorithm of the FullWAVE package. The 3D structures of the sensor were reduced to 2D structures by employing the effective index method [30] and numerical simulations with the 3D beam propagation method (BPM), included in the BeamPROP package. This is required in order to reduce the simulation time and allocated computer memory. Fig. 3(a) shows the spectral response calculated in the through port of the sensor for four distinct exposed areas of the disk (75%, 63%, 50% and 37%) and five different values of n_c in the sensing window. The schemes of each simulated sensor are inserted in the spectral response of Fig. 3(a), showing the percentage of the disk exposed area due to the presence of the sensing window (blue square). The black regions of these schemes represent the waveguides, ring and part of the disk, all covered by SiO_2 cladding, ensuring that the reference resonances are always fixed when n_c is changed in the sensing window.

The spectral responses show that the microring resonances are always fixed in the same wavelengths (λ_{Ref1} = 1606.23 nm and λ_{Ref2} = 1612.51 nm), regardless of the n_c used over the sensing window. Also, for all four cases of the exposed area of the disk, $\lambda_{detection}$ suffers a redshift when n_c is increased. These deviations among the detection resonances and λ_{Ref1} can be computed as $\Delta\lambda = |\lambda_{detection} - \lambda_{Ref1}|$. Fig. 3(b) shows the shift in the position of the detection resonance caused by the change in n_c, for different exposed areas of the disk, in percentage (a%). The linear fitting equations for each case are also shown and it can be seen that the slope of the curves, which corresponds to the sensor RI sensitivity (see Eq. 2), increases when the exposed area of the disk grows up. This can be clearly seen in Fig. 3(c), where the RI Sensitivity (S_{RI}) against the exposed area of the disk is presented. The linear fitting shows that the S_{RI} of the sensor increases by 0.222 nm / RIU when the percentage of the exposed area of the disk is increased by 1. This behavior of the S_{RI} with the variation of the exposed area is expected since the increase of the exposed area to the change in n_c favors a greater interaction of the disk propagating mode with the material in the sensing window, enhancing the S_{RI}.

We have also performed simulations to estimate a reliable operation range for this sensor where the coupling of the ring reference modes with the disk detection mode is not strong enough and can
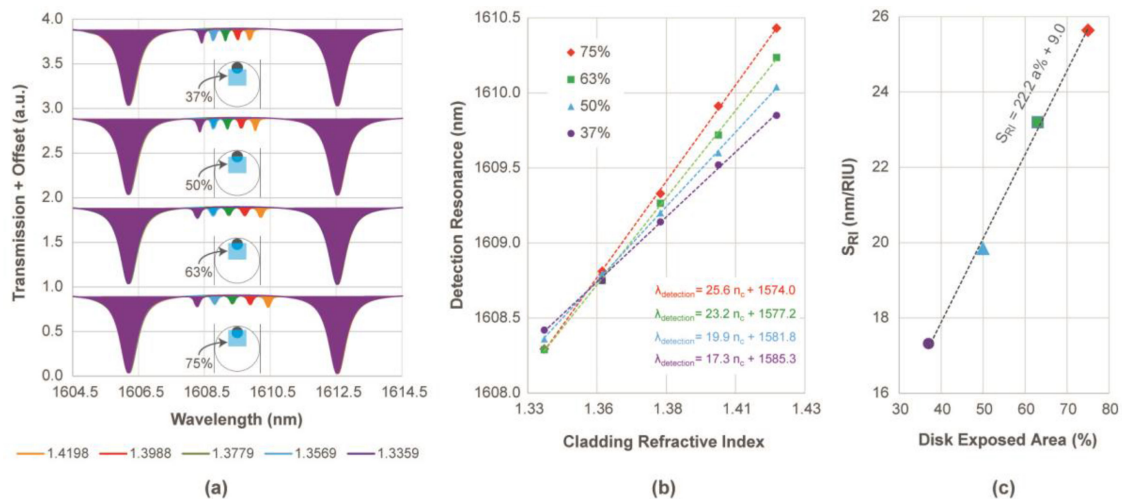
Fig. 3. (a) Spectral features of the sensor for four distinct disk exposed areas. In each condition, the clad refractive index is increased from 1.3359 (purple curve) to 1.4198 (orange curve). Inset: schematic view of the sensor highlighting the percentage value for the disk-exposed area. The sensing window is represented by the blue square, where distinct values of n_c are considered. (b) Resonant wavelength of the detection disk ($\lambda_{detection}$) against the cladding refractive index (n_c) in the sensing window. (c) Sensor sensitivity against the disk exposed area (a%). The dashed lines in (b) and (c) correspond to the linear fittings, including the fitted equations.

be neglected. Fig. 4(a) shows the detection resonance wavelength ($\lambda_{detection}$) and both reference resonance wavelengths (λ_{Ref1} and λ_{Ref2}) for a range of variation in the refractive index of the sensing window (Δn_c). The inset figures show the spectral region for the cases I, II and III, where there is significant coupling between the detection and reference resonant modes, potentially compromising the sensor's performance. However, it can be observed that the coupling between these modes is not strong enough and can be neglected in a Δn_c of approximately 0.15 RIU (light green region), which means that the sensor is operating in the non-degenerate condition in this particular region. Furthermore, this reliable Δn_c is greater than what it is expected experimentally because these sensors are projected to detect minimal refractive index changes less than 0.01 RIU in real life applications. Fig. 4(b) shows the sensor differential response ($\Delta\lambda = |\lambda_{detection} - \lambda_{Ref1}|$) against the Δn_c. The linear fitting shows that an RI sensitivity of (25.98 ± 2.13) nm/RIU is expected for this sensor in a reliable operation range of approximately 0.15 RIU (light green region). This simulation result is in agreement with the experimental value obtained in [7] for a single disk resonator. These results were obtained considering that 75% of the detection disk area is exposed, exactly like the sensor shown experimentally in the next section.

4. Experimental Results and Discussion

The experimental characterization of the fabricated sensor was performed as follows. A tunable laser (1465 nm to 1640 nm) was used as light source and the coupling of light into the waveguide was realized with GRIN rod lensed optical fibers. The transmitted light was collected using similar lenses and sent to an InGaAs power meter. The temperature was stabilized at 25°C and the input polarization was controlled to allow efficient coupling to the quasi-TE mode of the silicon waveguide. Fig. 5(a) shows the experimental transmission spectra of the sensor obtained for five aqueous EG solutions with different volume concentrations. In each case, the transmission spectrum of the sensor was measured after a droplet of approximately 0.5 μl of the prepared solution was applied on the sensor surface. The same experiment was repeated five times for each solution to secure the reliability of the developed sensor. The refractive indices of the aqueous EG solutions were
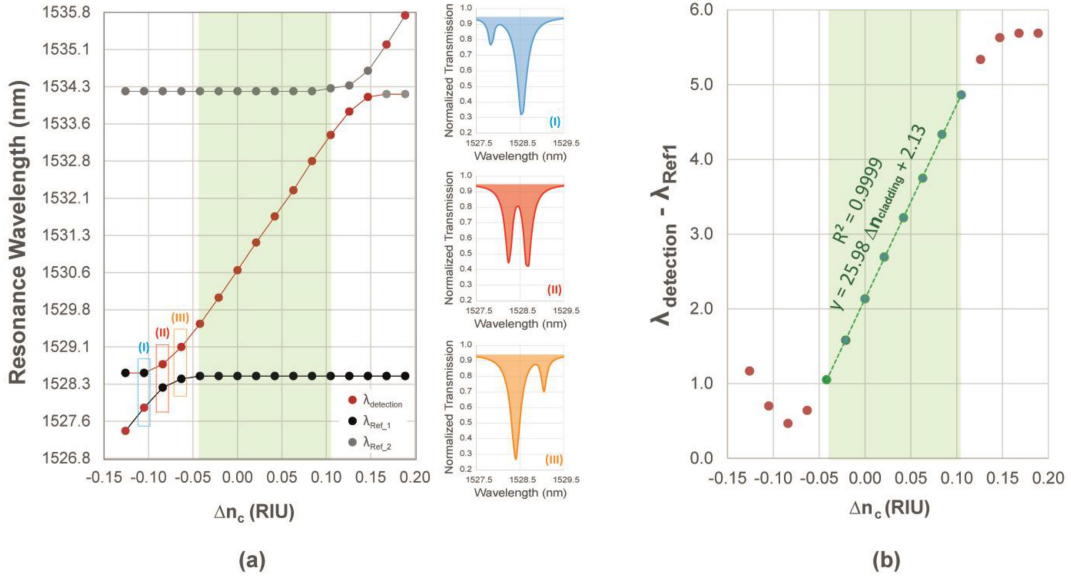
Fig. 4. (a) Detection resonance wavelength ($\lambda_{detection}$) and both reference resonances wavelength (λ_{Ref1} and λ_{Ref2}) plotted for a range of cladding refractive index. The inserted figures show the transmission spectrum close to λ_{Ref1} for the cases I, II, and III. The light green region corresponds to the reliable operation spectral range of the sensor. (b) Differential sensor response ($\Delta\lambda = |\lambda_{detection} - \lambda_{Ref1}|$) against the variation in n_c. The green dotted curve corresponds to the linear fitting of the reliable operation range.
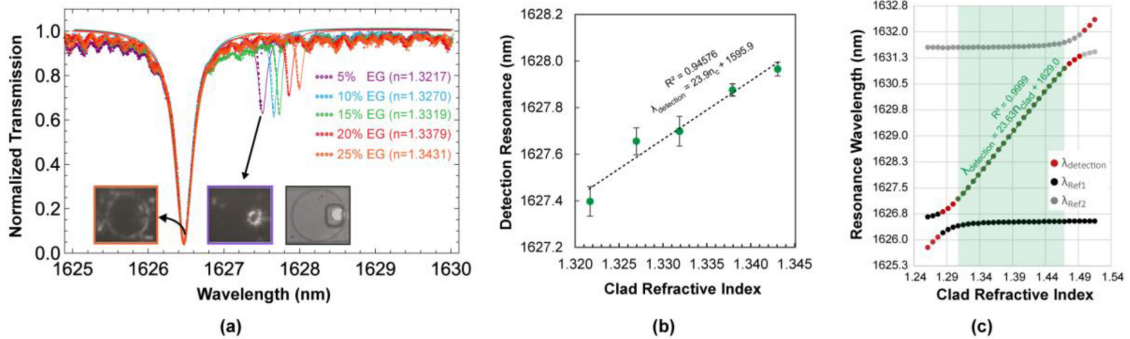

Fig. 5. (a) Fitted experimental spectra of the sensor for five aqueous EG solutions with distinct concentration. The inset figures are the infrared microscopy images of the scattered light in the resonances λ_{Ref1} and $\lambda_{detection}$, respectively. Also shown in the inset is the microcopy image of the fabricated sensor. (b) Detection resonance as a function of n_c in the sensing window. (c) Detection resonance ($\lambda_{detection}$) and both reference resonances (λ_{Ref1} and λ_{Ref2}) plotted against n_c extrapolated for other values. The dashed line in (b) and (c) correspond to the linear fittings with parameters shown.

obtained from [38] and the experimental spectrum for each case was fitted by the equation

$$T = \frac{-A_0 e^{j\Delta_0}\left(-A_1 e^{j\Delta_1} + t_1\right) + t_0\left(1 - A_1 e^{j\Delta_1} t_1\right)}{1 - A_1 e^{j\Delta_1} t_1 - A_0 e^{j\Delta_0}\left(-A_1 e^{j\Delta_1} + t_1\right)} \tag{9}$$

where T is the normalized transmission, and A_i and t_i represent, respectively, the loss and transmission coefficients for the external (indexed as 0) and internal (indexed as 1) cavities. The Δ_i's were obtained from the relation

$$\Delta_i = \frac{2\pi}{\lambda}\, n_{gi} L_i \tag{10}$$

where n_{gi} and L_i are, respectively, the group index and perimeter of cavity i. Equation 9 was obtained by the transfer matrix method (TMM).

The experimental spectral responses of the sensor (Fig. 5(a)) show that the reference resonance remained approximately fixed ($\lambda_{Ref1} \cong 1626.5$ nm) during the experiments. The inset figures show the corresponding infrared microscopy images of the scattered light in the resonances λ_{Ref1} ($\cong 1626.5$ nm) and $\lambda_{detection}$ ($\cong 1628$ nm). The microscopy image of the fabricated sensor is also presented to facilitate the identification of the resonant cavity at the pumped wavelength. These images demonstrate that when the laser is pumping in each resonant wavelength, the spatial distribution of the optical mode will be concentrated in the cavity associated with the resonance, as expected for a PM operating in the non-degenerated condition. During the sensor operation, the detection resonance suffered a redshift when the concentration of EG in water was increased. This redshift was caused by the increase of n_c in the sensing window from 5% ($n_c = 1.3217$) to 25% ($n_c = 1.3431$) and it is shown in detail in Fig. 5(b). The slope of the linear fitting shows an experimental sensitivity of $S_{RI} = (23.9 \pm 2.8)$ nm/RIU, giving a limit of detection LOD $\sim 1.7 \times 10^{-3}$ RIU, considering $Q \sim 40,000$. This result is in excellent agreement with our theoretical prediction for the RI sensitivity and is very close to the $S_{RI} = 27.1$ nm/RIU presented in reference [7] to a single disk sensor (R = 5 μm). However, our PM-based sensor has only 75% of the disk area susceptible to a change of n_c and it permits the presence of reference resonances requiring a reduced footprint (40 x 40 μm^2). Furthermore, the results show that there is no significant coupling between the detection and reference resonances because no resonant splitting can be observed in the detection resonances.

To estimate a reliable operation range for the application of the PM-based sensor, we used the fitted parameters of the experimental data to extrapolate the sensor spectral response for other values of n_c in the sensing window. Fig. 5(c) shows the detection resonance ($\lambda_{detection}$) and both reference resonances (λ_{Ref1} and λ_{Ref2}) against the extrapolated values of n_c. It can be observed that the detection resonance is practically linear between $n_c \approx 1.31$ and $n_c \approx 1.46$ (light green region), which corresponds to a change of approximately 0.15 RIU in the clad refractive index. Since an increase of 20% in the concentration of the EG solution corresponds to an increase of approximately 0.02 in the refractive index of this solution (see Fig. 5a), this reliable operating range of approximately 0.15 RIU is more than sufficient to guarantee the applicability of this sensor for aqueous solutions of higher concentrations.

The sensor differential response to temperature variations was evaluated by employing a temperature controller setup composed of a temperature controller (ILX-Lightwave–LDT-5525–Laser Diode Temperature Controller) and a Peltier (CP1.0-63-08L from Melcor). Fig. 6(a) shows the experimental transmission spectra obtained for four different temperatures with no solution applied to the sensing window. As expected, both the reference and detection resonances suffered a redshift when the temperature was increased. Furthermore, Fig. 6(b) shows that the resonance spectral shifts for the reference ring (blue) and detection disk (red) present very close sensitivities to temperature variations, (0.081 ± 0.001) nm/°C and (0.086 ± 0.003) nm/°C, respectively. Their sensitivities to temperature variations are not identical because 75% of the detection disk is exposed to the laboratory air and the SiO$_2$ cladding covers the other part, while the reference cavity is totally covered by the SiO$_2$ cladding. Now, considering the spectral shift of the sensor response (black), which is obtained by the differential measurement between the disk and ring resonances (See eq. 8), the sensitivity to temperature variation is reduced to (0.005 ± 0.002) nm/°C. This result shows that this PM-based sensor is about 16 times less sensitive to temperature variations than the reference resonances. In addition, it is less sensitive to temperature variations than previously published works employing single cavity sensor devices [12, 20].

Although the results obtained in this work with the different measurements are relevant, it is predictable that this sensor can potentially minimize the variation in its response with temperature fluctuations. This solution consists of reducing the exposed surface area of the detection cavity, allowing the detection and reference resonances to have even closer sensitivities to temperature variation. In this condition, the method of differential measurement presented in this work should be even more efficient. However, as shown in the sensing window simulations, there is a compromise
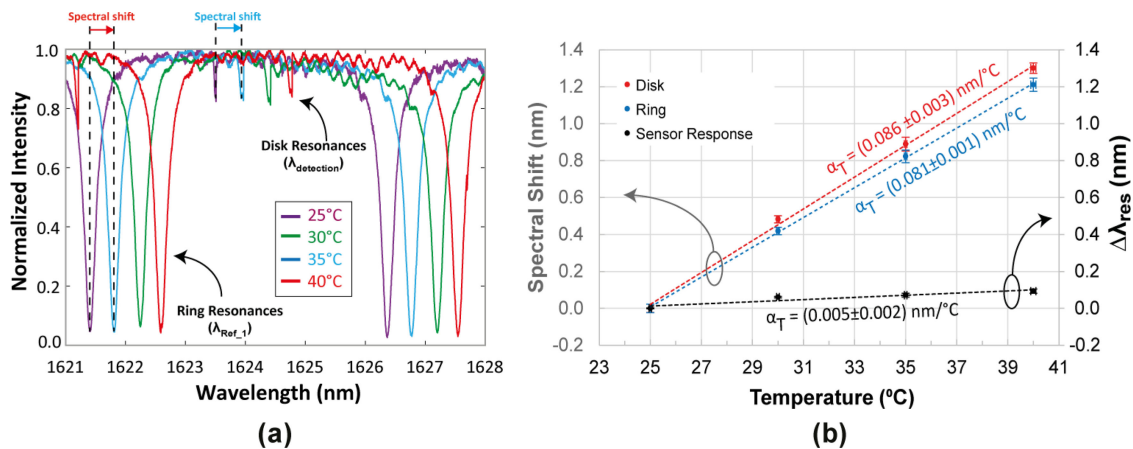
Fig. 6. (a) Experimental spectra of the sensor measured for four different temperatures. (b) Spectral shifts for the reference ring (blue) and detection disk (red) resonances as function of chip temperature. The black points represent the sensor differential response ($\Delta\lambda_{res}$) against chip temperature. The dashed lines are linear fittings and its related slopes are also shown.

between the size of the window and the sensitivity of the sensor. Reducing the exposed area of the disk will certainly cause a reduction in the sensitivity of the sensor. For this reason, in future work, new strategies should be presented to overcome this difficulty, reducing the window while maintaining both the sensitivity and compactness of the sensor.

5. Conclusion

We have demonstrated the design, fabrication and characterization of a sensor based on a PM that is composed of a microdisk internally coupled to a microring in a well-known add-drop filter configuration. In this sensor, only the inner microdisk is sensitive to changes in the top cladding refractive index and its resonance, non-degenerate with the microring resonances, has a high-Q ($\sim$40,000). One of these non-degenerate resonances was employed in the detection of different aqueous EG solutions by measuring its deviation from the reference resonances of the microring. An experimental RI sensitivity of (23.9 ± 2.8) nm/RIU was achieved with a LOD of approximately 1.7×10^{-3} RIU for a reliable operation range of 0.15 RIU in a compact footprint (40 μm $\times$ 40 μm). In addition, it was shown that the sensor response to temperature variations is about 16 times lower than the individual responses of the reference ring and the detection disk.

Acknowledgment

References

[1] K. J. Vahala, "Optical microcavities," *Nature*, vol. 424, no. 6950, Art. no. 6950, Aug. 2003, doi: 10.1038/nature01939.
[2] W. Bogaerts *et al.*, "Silicon microring resonators," *Laser & Photon. Rev.*, vol. 6, no. 1, pp. 47–73, Jan. 2012.
[3] V. M. N. Passaro, C. D. Tullio, B. Troia, M. L. Notte, G. Giannoccaro, and F. D. Leonardis, "Recent advances in integrated photonic sensors," *Sensors*, vol. 12, no. 11, Art. no. 11, Nov. 2012.
[4] Z. Yao *et al.*, "Integrated silicon photonic microresonators: Emerging technologies," *IEEE J. Sel. Topics Quantum Electronics*, vol. 24, no. 6, pp. 1–24, Nov. 2018.
[5] M.-K. Chin, C.-W. Lee, S.-Y. Lee, and S. Darmawan, "High-index-contrast waveguides and devices," *Appl. Opt.*, vol. 44, no. 15, pp. 3077–3086, May 2005.

[6] W. Bogaerts *et al.*, "Nanophotonic waveguides in silicon-on-insulator fabricated with CMOS technology," *J. Lightw. Technol.*, vol. 23, no. 1, pp. 401–412, Jan. 2005, doi: 10.1109/JLT.2004.834471.

[7] L. Chrostowski *et al.*, "Silicon photonic resonator sensors and devices," in *Laser Resonators, Microresonators, and Beam Control XIV*, Feb. 2012, vol. 8236, Art. no. 823620, doi: 10.1117/12.916860.

[8] E. Luan, H. Shoman, D. M. Ratner, K. C. Cheung, and L. Chrostowski, "Silicon photonic biosensors using label-free detection," *Sensors*, vol. 18, no. 10, Oct. 2018, Art. no. 3519, doi: 10.3390/s18103519.

[9] Z. Wang *et al.*, "Microfluidic channels with ultralow-loss waveguide crossings for various chip-integrated photonic sensors," *Opt. Lett.*, vol. 40, no. 7, pp. 1563–1566, Apr. 2015, doi: 10.1364/OL.40.001563.

[10] T. Lipka, L. Moldenhauer, L. Wahn, and H. K. Trieu, "Optofluidic biomolecule sensors based on a-Si: H microrings embedded in silicon–glass microchannels," *Opt. Lett.*, vol. 42, no. 6, pp. 1084–1087, Mar. 2017.

[11] M. c. Estevez, M. Alvarez, and L. m. Lechuga, "Integrated optical devices for lab-on-a-chip biosensing applications," *Laser & Photon. Rev.*, vol. 6, no. 4, pp. 463–487, 2012.

[12] W. N. Ye, R. Sun, J. Michel, L. Eldada, D. Pant, and L. C. Kimerling, "Thermo-optical compensation in high-index-contrast waveguides," in *Proc. 5th IEEE Int. Conf. Group IV Photon.*, Sep. 2008, pp. 401–403, doi: 10.1109/GROUP4.2008.4638214.

[13] J. Teng *et al.*, "Athermal Silicon-on-insulator ring resonators by overlaying a polymer cladding on narrowed waveg-uides," *Opt. Express*, vol. 17, no. 17, pp. 14627–14633, Aug. 2009, doi: 10.1364/OE.17.014627.

[14] M. Han and A. Wang, "Temperature compensation of optical microresonators using a surface layer with negative thermo-optic coefficient," *Opt. Lett.*, vol. 32, no. 13, pp. 1800–1802, Jul. 2007, doi: 10.1364/OL.32.001800.

[15] C. F. Carlborg *et al.*, "A packaged optical slot-waveguide ring resonator sensor array for multiplex label-free assays in labs-on-chips," *Lab Chip*, vol. 10, no. 3, pp. 281–290, Feb. 2010, doi: 10.1039/B914183A.

[16] D.-X. Xu *et al.*, "Real-time cancellation of temperature induced resonance shifts in SOI wire waveguide ring resonator label-free biosensor arrays," *Opt. Express*, vol. 18, no. 22, pp. 22867–22879, Oct. 2010, doi: 10.1364/OE.18.022867.

[17] K. B. Gylfason *et al.*, "On-chip temperature compensation in an integrated slot-waveguide ring resonator refractive index sensor array," *Opt. Express*, vol. 18, no. 4, pp. 3226–3237, Feb. 2010.

[18] D. Kim *et al.*, "On-chip integrated differential optical microring refractive index sensing platform based on a laminar flow scheme," *Opt. Lett.*, vol. 40, no. 17, pp. 4106–4109, Sep. 2015.

[19] W. N. Ye, J. Michel, and L. C. Kimerling, "Athermal high-index-contrast waveguide design," *IEEE Photon. Technol. Lett.*, vol. 20, no. 11, pp. 885–887, Jun. 2008.

[20] Linjie Zhou, K. Okamoto, and S. J. B. Yoo, "Towards athermal slotted silicon microring resonators with UV-trimmable PMMA upper-cladding," in *Proc. Conf. Lasers Electro-Optics 2009 Conf. Quantum Electron. Laser Sci. Conf.*, Jun. 2009, pp. 1–2.

[21] X. Zhou *et al.*, "An integrated photonic gas sensor enhanced by optimized fano effects in coupled microring resonators with an athermal waveguide," *J. Lightw. Technol.*, vol. 33, no. 22, pp. 4521–4530, Nov. 2015.

[22] Y. Temiz, R. D. Lovchik, G. V. Kaigala, and E. Delamarche, "Lab-on-a-chip devices: How to close and plug the lab?," *Microelectronic Engineering*, vol. 132, pp. 156–175, Jan. 2015.

[23] X. Chen, K. Huang, Z. Zeng, M. Zeng, C. Shen, and N. Bai, "A temperature sensor using cascaded microring resonators," *IOP Conf. Ser.: Mater. Sci. Eng.*, vol. 490, p. 072030, Apr. 2019.

[24] N. A. Yebo *et al.*, "Selective and reversible ammonia gas detection with nanoporous film functionalized silicon photonic micro-ring resonator," *Opt. Express*, vol. 20, no. 11, pp. 11855–11862, May 2012.

[25] A. Yalcin *et al.*, "Optical sensing of biomolecules using microring resonators," *IEEE J. Sel. Topics Quantum Electron.*, vol. 12, no. 1, pp. 148–155, Jan. 2006.

[26] G. A. Rodriguez, S. Hu, and S. M. Weiss, "Porous silicon ring resonator for compact, high sensitivity biosensing applications," *Opt. Express*, vol. 23, no. 6, pp. 7111–7119, Mar. 2015.

[27] Y. Zhang, T. Zhou, B. Han, A. Zhang, and Y. Zhao, "Optical bio-chemical sensors based on whispering gallery mode resonators," *Nanoscale*, vol. 10, no. 29, pp. 13832–13856, Jul. 2018.

[28] R. Guider *et al.*, "Sensitivity and limit of detection of biosensors based on ring resonators," *Sensing and Bio-Sensing Res.*, vol. 6, pp. 99–102, Dec. 2015.

[29] B. Su, C. Wang, Q. Kan, and C. HongDa, "Compact silicon-on-insulator dual-microring resonator optimized for sensing," *J. Lightw. Technol.*, vol. 29, no. 10, pp. 1535–1541, May 2011.

[30] L. A. M. Barea, F. Vallini, G. F. M. de Rezende, and N. C. Frateschi, "Spectral engineering with CMOS compatible SOI photonic molecules," *IEEE Photon. J.*, vol. 5, no. 6, Dec. 2013, Art. no. 2202717.

[31] L. A. M. Barea, F. Vallini, P. F. Jarschel, and N. C. Frateschi, "Silicon technology compatible photonic molecules for compact optical signal processing," *Appl. Phys. Lett.*, vol. 103, no. 20, p. 201102, Nov. 2013.

[32] M. C. M. M. Souza, G. F. M. Rezende, A. A. G. von Zuben, G. S. Wiederhecker, N. C. Frateschi, and L. a. M. Barea, "Tunable photonic molecules for spectral engineering in dense photonic integration," in *Future Trends in Microelectronics*, Wiley, 2016, pp. 337–348.

[33] L. A. M. Barea *et al.*, "Photonic molecules for application in silicon-on-insulator optical sensors," in *Silicon Photonics XIII*, Feb. 2018, vol. 10537, Art, no. 105371B, doi: 10.1117/12.2287844.

[34] L. a. M. Barea, F. Vallini, A. R. Vaz, J. R. Mialichi, and N. C. Frateschi, "Low-roughness active microdisk resonators fabricated by focused ion beam," *J. Vacuum Science Technol. B: Microelectronics Nanometer Structures Processing*, Measurement, and Phenomena, vol. 27, no. 6, pp. 2979–2981, Nov. 2009.

[35] F. Vallini, D. Figueira, P. Jarschel, L. Barea, A. A. von Zuben, and N. Frateschi, "Effects of ga+ milling on ingaasp quantum well laser with mirrors etched by focused ion beam," *J. Vacuum Science Technol. B: Microelectronics Nanometer Structures*, vol. 27, pp. L25–L27, Oct. 2009.

[36] J. R. Mialichi, L. A. M. Barea, P. L. D. Souza, R. M. S. Kawabata, M. P. Pires, and N. C. Frateschi, "Resonance modes in InAs/InGaAlAs/InP quantum dot microdisk resonators," *ECS Trans.*, vol. 31, no. 1, Oct. 2010, Art, no. 289.

[37] J. E. Saunders, C. Sanders, H. Chen, and H.-P. Loock, "Refractive indices of common solvents and solutions at 1550 nm," *Appl. Opt.*, vol. 55, no. 4, pp. 947–953, Feb. 2016.